Efficiency and Angular Distribution of Graphene-Plasmon Excitation by Electron Beam

Tetsuyuki Ochiai

Photonic Materials Unit, National Institute for Materials Science (NIMS), Tsukuba 305-0044, Japan

We theoretically study the efficiency and angular distribution of a graphene-plasmon excitation by an electron beam. An electron beam incident on doped graphene induces the out-of-plane transition radiation and in-plane plasmon-polariton waves. At the same time the electron loses its kinetic energy by energy conservation. From the momentum-resolved energy-loss spectrum, we can determine how much kinetic energy of the electron is converted into the transition radiation and plasmon-polariton excitation. Numerical results are presented by changing the incident angle and electron velocity. We find that the graphene plasmon polariton of particular frequency can be excited by an electron beam of appropriate velocity. Moreover, a deeply tilted incidence of the electron beam very efficiently excites the graphene plasmon polariton with an angular distribution range from −30 to 30 degrees. We also show that the transition radiation through graphene exhibits a peak at the threshold energy of the interband transition. These theoretical results are obtained under the local-response approximation of the optical conductivity as well as under the plasmon pole approximation. The results are also compared with those obtained in a thin metallic slab.

1. Introduction

Over the last few decades, various interesting phenomena using plasmons have been discovered in metallic nanostructures.[1,2] A plasmon, a collective excitation of many electrons,[3] couples with light, forming a coupled oscillation called a plasmon polariton. A plasmon polariton emerges as an eigenstate of light in metallic systems and can enhance various light-matter interactions. The enhancement is closely related to a subwavelength spatial profile of a plasmon polariton. For instance, a surface plasmon polariton localized in an interface between dielectric and metallic substances has a wave number $|\mathbf{k}_{\parallel}|$ much larger than the vacuum wave number ω/c.[4]

Recently, in addition to metallic systems, doped graphene in plasmonics has been receiving much attention.[5] It has free carriers obeying the Dirac spectrum and supports the sheet plasmon in it. Such a collective excitation enables the control of light in a one-monolayer-thick atomic membrane, and is now becoming an ultimate platform for plasmonics. Its potential is manifested by the perfect absorption of light and the vacuum Rabi splitting of an adsorbed molecule, which are theoretically predicted in patterned graphenes through a graphene plasmon polariton.[6,7]

Plasmon polaritons in patterned metallic and graphene nanostructures such as cavities, waveguides, and gratings, further exhibit complex subwavelength profiles whose length scales are much shorter than their vacuum wavelengths. Such a complex mode is difficult to excite selectively by optical means, because similar plasmon-polariton modes with different spatial profiles tend to degenerate with the mode under consideration. However, a selective excitation of a given plasmon-polariton mode is quite favorable for various applications, as the enhancement is not hidden by possible interference effects among degenerate modes.

An electron beam provides a solution to this problem. It is, after all, plasmon-friendly. Moreover, it can have a focusing-spot size on the order of Angstrom, much shorter than the subwavelength scale of the plasmon polariton under consideration.[8] A combination of electron-energy-loss spectroscopy (EELS) and optical spectroscopy in scanning transmission electron microscope (STEM) seems to be best-fitted to nanoscale plasmonic systems.

When a fast electron beam is incident on a plasmonic system, it excites a plasmon polariton, and radiation emission is induced. By energy conservation an incident electron loses its kinetic energy in this process. Momentum transfer is also observed between the beam and the plasmonic system. Therefore, the energy-loss and radiation-emission spectra, both in a momentum-resolved manner, provide detailed information on metallic and graphene nanostructures.[9]

Experimentally, momentum-resolved EELS is difficult to implement for small momenta far below atomic-scale momenta. However, momentum-resolved radiation-emission spectroscopy in a STEM setup has proven its advantages for various plasmonic systems.[10,11] EELS alone in STEM also provides deep insights into plasmonic systems.[12–14]

Historically, the interaction between an electron beam and a metal tends to be argued in two different contexts in physics. One is the solid-state physics context, where the nonretardation approximation is widely employed, and electron energy loss and nonretarded plasmon dispersion are of primary interest. The other is the beam physics context, where retardation is fully taken in account, and the properties of emitted lights (e.g., transition radiation,[15] Cherenkov radiation,[16] bremsstrahlung, and Smith-Purcell radiation[17]) are of primary interest. Here, we deal with the two contexts in a unified manner, by employing a retarded approach to EELS. Retardation is inevitably accompanied by radiation emission. Thus, the energy-loss and radiation-emission spectra can be dealt with on an equal footing.

In this paper, we present theoretical results of the electron energy-loss and transition-radiation spectra in the local-response approximation of the optical conductivity of doped graphene. The plasmon pole approximation[18] is also employed to evaluate the excitation efficiency and angular distribution of the graphene plasmon polariton. For comparison,

we also consider similar quantities in a thin metallic slab, and compare the results with those of doped graphene. The ultimate thickness of such graphene exhibits a marked contrast to that of the metallic slab.

This paper is organized as follows. In Sect. 2 we present a basic theoretical framework for graphene optical responses as well as the interaction with the electron beam transmitted through graphene. We summarize a corresponding theory for homogeneous slabs in Sect. 3. In Sect. 4 we present numerical results of the electron-energy-loss and transition-radiation spectra, the excitation rates of a plasmon polariton, and the angular distributions of a plasmon polariton as well as the transition radiation in doped graphene. We also compare the results with those in a thin metallic slab. We give the conclusions drawn in Sect. 5. In Appendix, we present the energy-loss spectra for an electron traveling parallel to graphene, as an extreme case.

2. Graphene

2.1 Optical response of graphene

Let us model graphene as an infinitely thin electrically conducting sheet placed at $z = 0$. For simplicity, we assume a local response in conductivity, so that the induced two-dimensional (2d) current $j_\parallel(x_\parallel)$ is given by $\overleftrightarrow{\sigma} E_\parallel(x_\parallel)$ with the spatially independent conductivity $\overleftrightarrow{\sigma}$ and the in-plane electric field $E_\parallel(x_\parallel)$. In the optical regime, this current can be regarded as the polarization current. Therefore, graphene can also be modeled with a dipole sheet with polarizability $\overleftrightarrow{\alpha}^0|_{2d} = i\overleftrightarrow{\sigma}/\omega$. In principle, graphene can have the out-of-plane polarizability in addition to the in-plane polarizability $\overleftrightarrow{\alpha}^0|_{2d}$. However, the out-of-plane components (the xz, yz, zz, zx, and zy components) are generally small, taking account of the selection rule of the π orbitals of graphene. Near the Fermi level, valence and conduction bands are of the π band, whose atomic orbital has the p_z symmetry. Therefore, dipole matrix elements relevant to the out-of-plane polarizability, namely, $\langle 0|z|n\rangle$ ($|0\rangle$ and $|n\rangle$, which are the ground state and an intermediate state, respectively, in the Kramers-Heisenberg formula of the conductivity) vanish because of the symmetry. In what follows, we thus neglect the out-of-plane components of the polarizability.

Since graphene can be regarded as a dipole sheet, light scattering by graphene is nothing but Rayleigh scattering. Suppose a time-harmonic incident light $E^0(x) = E_k^0(z) \exp(ik_\parallel \cdot x_\parallel)$ is coming to the dipole sheet. This light is then scattered by the dipole sheet. The Maxwell equation that describes the scattering is given by

$$\nabla \times E(x) = i\omega B(x), \tag{1}$$

$$\nabla \times H(x) = -i\omega(D(x) + P_{ds}(x)), \tag{2}$$

$$D(x) = \epsilon_0 \epsilon_b E(x), \quad H(x) = \frac{1}{\mu_0} B(x), \quad P_{ds}(x) = \overleftrightarrow{\alpha}^0 E(x)\delta(z), \tag{3}$$

where ϵ_b is the permittivity of the background medium, and P_{ds} is the induced polarization in the dipole sheet. The harmonic time dependence $\exp(-i\omega t)$ of the angular frequency ω is omitted from the electromagnetic field. Therefore, the electric field satisfies

$$\nabla \times \nabla \times E(x) = q_b^2 E(x) + \mu_0 \omega^2 P_{ds}(x), \tag{4}$$

with $q_b = (\omega/c)\sqrt{\epsilon_b}$. Using the Green function G of the Helmholtz equation, the above equation is written as

$$E(x) = E^0(x) + \mu_0\omega^2 \int d^3x' \overleftrightarrow{G}(x, x') P_{ds}(x'), \tag{5}$$

$$\overleftrightarrow{G}(x, x') = -\left(\overleftrightarrow{1} + \frac{1}{q_b^2}\nabla \otimes \nabla\right)G(x, x'), \tag{6}$$

$$(\Delta + q_b^2)G(x, x') = \delta^{(3)}(x - x'). \tag{7}$$

The Green function has the Fourier-expansion form given by

$$G(x, x') = \int \frac{d^2k_\parallel}{(2\pi)^2} e^{ik_\parallel \cdot (x_\parallel - x_\parallel')} \frac{1}{2i\gamma_b} e^{i\gamma_b|z-z'|}, \tag{8}$$

with $\gamma_b = \sqrt{q_b^2 - k_\parallel^2}$.

By the translational invariance in plane, the total electric field (incident plus induced fields) is written as

$$E(x) = E_k(z)e^{ik_\parallel \cdot x_\parallel}, \tag{9}$$

$$E_k(z) = E_k^0(z) + t^\pm e^{i\gamma_b|z|} - \frac{1}{\epsilon_0 \epsilon_b}\delta(z)\hat{z} \otimes \hat{z}\overleftrightarrow{\alpha}^0 E_k(0), \tag{10}$$

$$t^\pm = -\left(\overleftrightarrow{1} - \frac{1}{q_b^2}K_b^\pm \otimes K_b^\pm\right)\overleftrightarrow{\alpha}^0 E_k(0), \tag{11}$$

$$\overleftrightarrow{\alpha}^0 = \frac{\mu_0\omega^2}{2i\gamma_b}\overleftrightarrow{\alpha}^0, \tag{12}$$

$$K_b^\pm = k_\parallel \pm \gamma_b\hat{z}. \tag{13}$$

The superscript $\pm$ of t refers to the sign of z. The second and third terms in Eq. (10) both stand for the induced field. The former term is a propagating one, while the latter remains in the dipole sheet.

We should note that the propagating field is completely symmetric with respect to $z = 0$, provided that the out-of-plane polarizability components vanish. In fact, we have $t_p^+ = t_p^-$ and $t_s^+ = t_s^-$, where $t_{p(s)}^\pm$ is the p(s) polarization component of $t^\pm$:

$$t^\pm = t_p^\pm p_b^\pm + t_s^\pm s, \tag{14}$$

$$p_b^\pm = \pm\frac{\gamma_b}{q_b}\hat{k}_\parallel - \frac{|k_\parallel|}{q_b}\hat{z}, \quad s = \hat{k}_\perp, \tag{15}$$

$$\hat{k}_\parallel = \left(\frac{k_x}{|k_\parallel|}, \frac{k_y}{|k_\parallel|}, 0\right), \quad k_\perp = \left(-\frac{k_y}{|k_\parallel|}, \frac{k_x}{|k_\parallel|}, 0\right). \tag{16}$$

This implies that the same amount of induced wave is obtained above and below graphene, irrespective of the incident wave.

Taking account of radiation damping, we introduce the effective polarizability $\overleftrightarrow{\alpha}_k$ as[19]

$$\overleftrightarrow{\alpha}_k = \overleftrightarrow{\alpha}^0\left(\overleftrightarrow{M}_k\right)^{-1}, \tag{17}$$

$$\overleftrightarrow{M}_k = \overleftrightarrow{1} + \left(\overleftrightarrow{1} - \frac{1}{q_b^2}k_\parallel \otimes k_\parallel - \frac{\gamma_b^2}{q_b^2}\hat{z} \otimes \hat{z}\right)\overleftrightarrow{\alpha}^0, \tag{18}$$

from which we have

$$\overleftrightarrow{\alpha}^0 E_k(0) = \overleftrightarrow{\alpha}_k E_k^0(0), \tag{19}$$

and the optical theorem holds.

The matrix inverse in Eq. (17) has a pole due to the graphene plasmon polariton. Let us assume the rotational in-
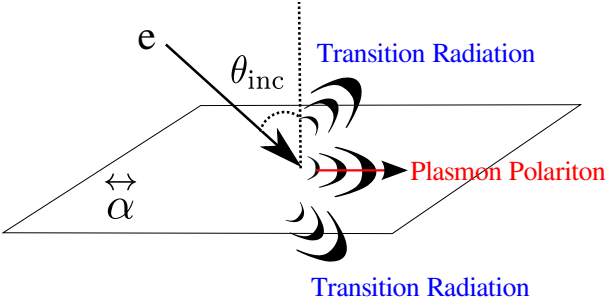
Fig. 1. (Color online) Schematic illustration of the system under study. The electron beam incident on the graphene sheet induces the out-of-plane transition radiation and the in-plane plasmon-polariton waves.

variance of graphene. The polarizability thus satisfies $\alpha_{xx}^0 = \alpha_{yy}^0$ and $\alpha_{xy}^0 = -\alpha_{yx}^0$. The dispersion relation of the graphene plasmon polariton is given by the vanishing determinant of the matrix $\overleftrightarrow{M}_k$. Therefore, it is the solution of

$$\det \overleftrightarrow{M}_k = (1 + \tilde{\alpha}_{xx}^0)\left(1 + \frac{\gamma_b^2}{q_b^2}\tilde{\alpha}_{xx}^0\right) + \left(\frac{\gamma_b}{q_b}\tilde{\alpha}_{xy}^0\right)^2 = 0. \quad (20)$$

The graphene plasmon polariton very strongly affects the light-matter interaction in doped graphene.

2.2 Interaction with electron beam

When an electron beam transmits through graphene, it induces out-of-plane transition radiation. At the same time, the electron excites in-plane graphene plasmon polaritons. As a result, the incident electron loses its kinetic energy. Let us suppose a high-energy electron beam. The energy loss is then very small compared with the kinetic energy, so that the recoil of the electron is fairly neglected. A schematic illustration of the system under study is shown in Fig. 1.

The electric field accompanied by a traveling electron with charge e and velocity $\boldsymbol{v}$ is written as[20]

$$\boldsymbol{E}^0(\boldsymbol{x}, t) = \int_{-\infty}^{\infty} \frac{d\omega}{2\pi} e^{-i\omega t} \boldsymbol{E}^0(\boldsymbol{x}; \omega), \quad (21)$$

$$\boldsymbol{E}^0(\boldsymbol{x}; \omega) = \int \frac{d^2\boldsymbol{k}_\parallel}{(2\pi)^2} e^{i\boldsymbol{k}_\parallel \cdot \boldsymbol{x}_\parallel} \boldsymbol{E}_k^0(z; \omega), \quad (22)$$

$$\boldsymbol{E}_k^0(z; \omega) = \frac{-i\mu_0 e\omega}{q_b^2 - \boldsymbol{K}_v^2} \boldsymbol{P}_v e^{ik_{zv}z}, \quad (23)$$

$$\boldsymbol{P}_v = \left(\overleftrightarrow{1} - \frac{1}{q_b^2}\boldsymbol{K}_v \otimes \boldsymbol{K}_v\right)\frac{\boldsymbol{v}}{v_z} = \frac{\omega}{q_b^2 v_z}\left(\frac{\omega\epsilon_b}{c^2}\boldsymbol{v} - \boldsymbol{K}_v\right), \quad (24)$$

$$\boldsymbol{K}_v = (k_x, k_y, k_{zv}), \quad k_{zv} = \frac{\omega - k_x v_x - k_y v_y}{v_z}. \quad (25)$$

The energy loss $-\Delta E$ ($\Delta E < 0$) of the electron after transmitting through graphene is written as

$$-\Delta E = -e \int_{-\infty}^{\infty} dt \boldsymbol{v} \cdot \boldsymbol{E}(\boldsymbol{x}_t, t),$$

$$= \int_0^{\infty} d\omega \hbar\omega \Gamma_{\text{EL}}(\omega), \quad (26)$$

$$\Gamma_{\text{EL}}(\omega) = -\frac{e}{\pi\hbar\omega}\Re\left[\int_{-\infty}^{\infty} dt e^{-i\omega t} \boldsymbol{v} \cdot \boldsymbol{E}(\boldsymbol{x}_t; \omega)\right]$$

$$= \int \frac{d^2\boldsymbol{k}_\parallel}{(2\pi)^2}\Gamma_{\text{EL}}(\omega, \boldsymbol{k}_\parallel), \quad (27)$$

$$\Gamma_{\text{EL}}(\omega, \boldsymbol{k}_\parallel) = \frac{2\mu_0 e^2}{\pi\hbar}\Re\left[\frac{\gamma_b}{(q_b^2 - \boldsymbol{K}_v^2)^2}\boldsymbol{P}_v^t \overleftrightarrow{\tilde{\alpha}}_k \boldsymbol{P}_v\right], \quad (28)$$

$$\overleftrightarrow{\tilde{\alpha}}_k = \frac{\mu_0\omega^2}{2i\gamma_b}\overleftrightarrow{\alpha}_k, \quad (29)$$

where $\Gamma_{\text{EL}}(\omega, \boldsymbol{k}_\parallel)$ is the momentum-resolved energy-loss spectrum, and $\boldsymbol{x}_t = \boldsymbol{v}t$ is the electron position at time t. Here, we assume that no Cherenkov loss takes place in the background medium.[21] The momentum change $\Delta\boldsymbol{p}_\parallel$ of the electron in the direction parallel to graphene is given by

$$-\Delta\boldsymbol{p}_\parallel = \int_0^{\infty} d\omega \int \frac{d^2\boldsymbol{k}_\parallel}{(2\pi)^2}\hbar\boldsymbol{k}_\parallel\Gamma_{\text{EL}}(\omega, \boldsymbol{k}_\parallel). \quad (30)$$

Therefore, $\Gamma_{\text{EL}}(\omega, \boldsymbol{k}_\parallel)$ represents the differential probability of the energy loss $\hbar\omega$ and the momentum transfer $\hbar\boldsymbol{k}_\parallel$.

On the other hand, the transition-radiation energy W (total radiation energy emitted from graphene) out of plane is given by

$$W = \int_{-\infty}^{\infty} dt \int d\boldsymbol{S} \cdot \boldsymbol{E}(\boldsymbol{x}, t) \times \boldsymbol{H}(\boldsymbol{x}, t)$$

$$= \int_0^{\infty} d\omega \hbar\omega \Gamma_{\text{TR}}(\omega), \quad (31)$$

$$\Gamma_{\text{TR}}(\omega) = \frac{1}{\pi\hbar\omega}\Re\left[\int d\boldsymbol{S} \cdot \boldsymbol{E}^*(\boldsymbol{x}; \omega) \times \boldsymbol{H}(\boldsymbol{x}; \omega)\right]$$

$$= \int_{|\boldsymbol{k}_\parallel|<q_b} \frac{d^2\boldsymbol{k}_\parallel}{(2\pi)^2}\Gamma_{\text{TR}}(\omega, \boldsymbol{k}_\parallel), \quad (32)$$

$$\Gamma_{\text{TR}}(\omega, \boldsymbol{k}_\parallel) = \frac{1}{\pi\hbar\omega}\frac{\gamma_b}{\mu_0\omega}(|t^+|^2 + |t^-|^2). \quad (33)$$

Here, the surface integral of the Poynting vector is taken at $z = \pm\infty$, so that all evanescent waves propagating graphene in plane are omitted. The momentum-resolved transition-radiation spectrum $\Gamma_{\text{TR}}(\omega, \boldsymbol{k}_\parallel)$ is proportional to the differential cross section of the transition radiation as

$$\frac{\partial^2 W}{\partial(\hbar\omega)\partial\Omega} = \frac{\omega q_b^2 \cos\theta}{2(2\pi)^2}\Gamma_{\text{TR}}(\omega, \boldsymbol{k}_\parallel), \quad (34)$$

$$k_x = q_b \sin\theta\cos\phi, \quad k_y = q_b \sin\theta\sin\phi, \quad (35)$$

where $\Omega = (\theta, \phi)$ is the solid angle.

Although the Planck's constant appears in the above expressions, it is just for a quantum-mechanical interpretation. All the calculations performed in this paper are fully classical, provided that the quantum-mechanical polarizability is given.

We can show that, for dissipation-less graphene (hermitian $\overleftrightarrow{\alpha}^0$), the momentum-resolved energy-loss spectrum $\Gamma_{\text{EL}}(\omega, \boldsymbol{k}_\parallel)$ is a delta function outside the light cone. Inside the light cone, it is equal to the transition-radiation spectrum $\Gamma_{\text{TR}}(\omega, \boldsymbol{k}_\parallel)$. The delta function stands for the excitation of the graphene plasmon polariton. Thus,

$$\Gamma_{\text{EL}}^{\text{pp}}(\omega) = \int_{|\boldsymbol{k}_\parallel|>q_b} \frac{d^2\boldsymbol{k}_\parallel}{(2\pi)^2}\Gamma_{\text{EL}}(\omega, \boldsymbol{k}_\parallel), \quad (36)$$

namely, the energy-loss spectrum outside the light cone, provides information up to extent at which the graphene plasmon

polariton is excited by the electron beam. Similarly,

$$\Gamma_{\text{EL}}^{\text{tr}}(\omega) = \int_{|\boldsymbol{k}_\parallel| < q_b} \frac{d^2\boldsymbol{k}_\parallel}{(2\pi)^2} \Gamma_{\text{EL}}(\omega, \boldsymbol{k}_\parallel), \tag{37}$$

provides how much the electron beam induces transition radiation.

In a normal incident case, $\Gamma_{\text{EL}}(\omega, \boldsymbol{k}_\parallel)$ is a function of $|\boldsymbol{k}_\parallel|$ by rotational invariance. However, in an oblique-incidence case, $\Gamma_{\text{EL}}(\omega, \boldsymbol{k}_\parallel)$ depends on $\arg(\boldsymbol{k}_\parallel) \equiv \phi_{\boldsymbol{k}}$. Important information is thus found in

$$\Gamma_{\text{EL}}^{\text{pp}}(\omega, \phi_{\boldsymbol{k}}) = \int_{q_b}^{\infty} \frac{dk_\parallel k_\parallel}{2\pi} \Gamma_{\text{EL}}(\omega, \boldsymbol{k}_\parallel), \tag{38}$$

which represents the angular distribution of the graphene plasmon polariton at a frequency ω.

To confirm the delta-function dependence, we note that Eq. (28) can be written as

$$\Gamma_{\text{EL}}(\omega, \boldsymbol{k}_\parallel) = \frac{\mu_0 e^2}{\pi\hbar} \frac{\gamma_b}{q_b^2 - \boldsymbol{K}_v^2} \boldsymbol{P}_v^t (\overleftrightarrow{\alpha}_{\boldsymbol{k}} - \overleftrightarrow{\alpha}_{\boldsymbol{k}}^\dagger) \boldsymbol{P}_v, \tag{39}$$

outside the light cone with a pure imaginary γ_b. Naively, $\overleftrightarrow{\alpha}_{\boldsymbol{k}}$ is shown to be hermite for dissipation-less graphene, so that $\Gamma_{\text{EL}}(\omega, \boldsymbol{k}_\parallel)$ seems to vanish. However, there is an exception at the pole of $\overleftrightarrow{\alpha}_{\boldsymbol{k}}$, which corresponds to the graphene plasmon polariton. Around the pole, the determinant of $\overleftrightarrow{M}_{\boldsymbol{k}}$ is written as

$$\det \overleftrightarrow{M}_{\boldsymbol{k}} \simeq \lambda(k_\parallel - k_\parallel^{\text{pp}}(\omega) - i\varepsilon). \tag{40}$$

Here, ε is an infinitesimal positive number that explains the causality (the Sommerfeld radiation condition),[22] and $k_\parallel = k_\parallel^{\text{pp}}(\omega)$ is the dispersion relation of the graphene plasmon polariton. Therefore, we have

$$\overleftrightarrow{\alpha}_{\boldsymbol{k}} - \overleftrightarrow{\alpha}_{\boldsymbol{k}}^\dagger = \overleftrightarrow{\alpha}^0 \overleftrightarrow{C}_{\boldsymbol{k}} \frac{2\pi i}{\lambda} \delta(k_\parallel - k_\parallel^{\text{pp}}(\omega)), \tag{41}$$

where $\overleftrightarrow{C}_{\boldsymbol{k}}$ is the cofactor of $\overleftrightarrow{M}_{\boldsymbol{k}}$. This delta-function profile enables us to almost analytically (the $\phi_{\boldsymbol{k}}$ integration is still left) evaluate the excitation rate $\Gamma_{\text{EL}}^{\text{pp}}(\omega)$ of the graphene plasmon polariton. As for the contribution of the transition-radiation rate $\Gamma_{\text{EL}}^{\text{tr}}(\omega)$, we need to perform a numerical integration over $\boldsymbol{k}_\parallel$ inside the light cone.

3. Homogeneous Slab

For comparison, we consider an electron beam interacting with a homogeneous slab. In a dielectric slab, slab guided modes play a significant role in the interaction. In a metallic slab, the Ritchie plasmon-polariton modes[23] dominate the interaction. In a slab case, a standard approach to solving light scattering and EELS problems is the layer-by-layer method.[24] Although this method is well known, we briefly summarize the theory of the EELS just for notational convenience.

Suppose a homogeneous slab of permittivity ϵ_a and thickness d is embedded in an outer medium of permittivity ϵ_b. The incident electron from the top induces the transmitted and reflected waves in the lower and upper regions, respectively. The total electric field becomes

$$\boldsymbol{E}(\boldsymbol{x}; \omega) = \int \frac{d^2\boldsymbol{k}_\parallel}{(2\pi)^2} e^{i\boldsymbol{k}_\parallel \cdot \boldsymbol{x}_\parallel} \boldsymbol{E}_{\boldsymbol{k}}(z; \omega), \tag{43}$$

$$\boldsymbol{E}_{\boldsymbol{k}}(z; \omega) = \begin{cases} \boldsymbol{E}_{\boldsymbol{k}}^{0b}(z; \omega) + \boldsymbol{E}_{\boldsymbol{k}}^+(z; \omega) & z > \frac{d}{2}, \\ \boldsymbol{E}_{\boldsymbol{k}}^{0a}(z; \omega) + \boldsymbol{E}_{\boldsymbol{k}}^{\text{ins}}(z; \omega) & |z| < \frac{d}{2}, \\ \boldsymbol{E}_{\boldsymbol{k}}^{0b}(z; \omega) + \boldsymbol{E}_{\boldsymbol{k}}^-(z; \omega) & z < -\frac{d}{2}, \end{cases} \tag{44}$$

$$\boldsymbol{E}_{\boldsymbol{k}}^\pm(z; \omega) = (t_p^\pm \boldsymbol{p}_b^\pm + t_s^\pm \boldsymbol{s}) e^{\pm i\gamma_b z}, \tag{45}$$

$$\boldsymbol{E}_{\boldsymbol{k}}^{\text{ins}}(z; \omega) = (c_p^+ \boldsymbol{p}_a^+ + c_s^+ \boldsymbol{s}) e^{i\gamma_a z} + (c_p^- \boldsymbol{p}_a^- + c_s^- \boldsymbol{s}) e^{-i\gamma_a z}, \tag{46}$$

where $\boldsymbol{E}_{\boldsymbol{k}}^{0b}$ is nothing but Eq. (23), and $\boldsymbol{E}_{\boldsymbol{k}}^{0a}$ is obtained simply by replacing ϵ_b with ϵ_a in Eq. (23). By imposing the boundary conduction at $z = \pm d/2$, the unknown coefficients $t_p^\pm, t_s^\pm, c_p^\pm,$ and $c_s^\pm$ are solved as follows.

$$\begin{pmatrix} \left(\frac{\gamma_a}{q_a^2} - \frac{\gamma_b}{q_b^2}\right) e^{i\gamma_a \frac{d}{2}} & -\left(\frac{\gamma_a}{q_a^2} + \frac{\gamma_b}{q_b^2}\right) e^{-i\gamma_a \frac{d}{2}} \\ \left(\frac{\gamma_a}{q_a^2} + \frac{\gamma_b}{q_b^2}\right) e^{-i\gamma_a \frac{d}{2}} & -\left(\frac{\gamma_a}{q_a^2} - \frac{\gamma_b}{q_b^2}\right) e^{i\gamma_a \frac{d}{2}} \end{pmatrix} \begin{pmatrix} c_p^+ \\ c_p^- \end{pmatrix} = \begin{pmatrix} J_p^+ \\ J_p^- \end{pmatrix}, \tag{47}$$

$$\begin{pmatrix} (\gamma_a - \gamma_b) e^{i\gamma_a \frac{d}{2}} & -(\gamma_a + \gamma_b) e^{-i\gamma_a \frac{d}{2}} \\ (\gamma_a + \gamma_b) e^{-i\gamma_a \frac{d}{2}} & -(\gamma_a - \gamma_b) e^{i\gamma_a \frac{d}{2}} \end{pmatrix} \begin{pmatrix} c_s^+ \\ c_s^- \end{pmatrix} = \begin{pmatrix} J_s^+ \\ J_s^- \end{pmatrix}, \tag{48}$$

$$J_p^\pm = \frac{i\mu_0 e\omega}{q_a} \left[\frac{1}{q_a^2 - \boldsymbol{K}_v^2} \left(\frac{\boldsymbol{v} \cdot \hat{\boldsymbol{k}}_\parallel}{v_z} - \frac{\omega|\boldsymbol{k}_\parallel|}{v_z q_a^2}\right) - \frac{1}{q_b^2 - \boldsymbol{K}_v^2} \left(\frac{\boldsymbol{v} \cdot \hat{\boldsymbol{k}}_\parallel}{v_z} - \frac{\omega|\boldsymbol{k}_\parallel|}{v_z q_b^2}\right) \right.$$
$$\left. \pm \frac{\gamma_b}{q_b^2} \left(\frac{1}{q_a^2 - \boldsymbol{K}_v^2} - \frac{1}{q_b^2 - \boldsymbol{K}_v^2}\right) \left(|\boldsymbol{k}_\parallel| - \frac{k_{zv}\boldsymbol{v} \cdot \hat{\boldsymbol{k}}_\parallel}{v_z}\right) \right] e^{\pm ik_{zv}\frac{d}{2}}, \tag{49}$$

$$J_s^\pm = i\mu_0 e\omega \left(\frac{1}{q_a^2 - \boldsymbol{K}_v^2} - \frac{1}{q_b^2 - \boldsymbol{K}_v^2}\right) \frac{\boldsymbol{v} \cdot \hat{\boldsymbol{k}}_\perp}{v_z} (k_{zv} \mp \gamma_b) e^{\pm ik_{zv}\frac{d}{2}}, \tag{50}$$

$$t_p^\pm = \frac{q_b}{\gamma_b} e^{-i\gamma_b \frac{d}{2}} \left\{ \pm \frac{\gamma_a}{q_a}(c_p^+ e^{\pm i\gamma_a \frac{d}{2}} - c_p^- e^{\mp i\gamma_a \frac{d}{2}}) \right.$$
$$\left. - i\omega\mu_0 e \left[\frac{1}{q_a^2 - \boldsymbol{K}_v^2}\left(\frac{\boldsymbol{v} \cdot \hat{\boldsymbol{k}}_\parallel}{v_z} - \frac{\omega|\boldsymbol{k}_\parallel|}{v_z q_a^2}\right) - \frac{1}{q_b^2 - \boldsymbol{K}_v^2}\left(\frac{\boldsymbol{v} \cdot \hat{\boldsymbol{k}}_\parallel}{v_z} - \frac{\omega|\boldsymbol{k}_\parallel|}{v_z q_b^2}\right)\right] e^{\pm ik_{zv}\frac{d}{2}} \right\}, \tag{51}$$

$$t_s^{\pm} = e^{-i\gamma_b \frac{d}{2}} \left[c_s^+ e^{\pm i\gamma_a \frac{d}{2}} + c_s^- e^{\mp i\gamma_a \frac{d}{2}} - i\mu_0 e\omega \left(\frac{1}{q_a^2 - K_v^2} - \frac{1}{q_b^2 - K_v^2} \right) \frac{\boldsymbol{v} \cdot \hat{\boldsymbol{k}}_{\perp}}{v_z} e^{\pm ik_{zv} \frac{d}{2}} \right]. \qquad (52)$$

By using the above solution, the energy-loss and transition-radiation spectra are obtained as

$$\Gamma_{\mathrm{EL}}(\omega, \boldsymbol{k}_{\parallel}) = -\frac{e}{\pi\hbar\omega} \Re \left[\boldsymbol{v} \cdot (t_p^+ \boldsymbol{p}_b^+ + t_s^+ \boldsymbol{s}) \frac{e^{i(\gamma_b - k_{zv})\frac{d}{2}}}{i(\omega - \boldsymbol{K}_b^+ \cdot \boldsymbol{v})} \right.$$

$$- \boldsymbol{v} \cdot (t_p^- \boldsymbol{p}_b^- + t_s^- \boldsymbol{s}) \frac{e^{i(\gamma_b + k_{zv})\frac{d}{2}}}{i(\omega - \boldsymbol{K}_b^- \cdot \boldsymbol{v})}$$

$$- \boldsymbol{v} \cdot (c_p^+ \boldsymbol{p}_a^+ + c_s^+ \boldsymbol{s}) \frac{e^{i(\gamma_a - k_{zv})\frac{d}{2}} - e^{-i(\gamma_a - k_{zv})\frac{d}{2}}}{i(\omega - \boldsymbol{K}_a^+ \cdot \boldsymbol{v})}$$

$$- \boldsymbol{v} \cdot (c_p^- \boldsymbol{p}_a^- + c_s^- \boldsymbol{s}) \frac{e^{-i(\gamma_a + k_{zv})\frac{d}{2}} - e^{i(\gamma_a + k_{zv})\frac{d}{2}}}{i(\omega - \boldsymbol{K}_a^- \cdot \boldsymbol{v})}$$

$$\left. - i\omega\mu_0 ed \frac{\frac{|\boldsymbol{v}|^2}{v_z^2} - \frac{\omega^2}{v_z^2 q_a^2}}{q_a^2 - K_v^2} \right], \qquad (53)$$

$$\Gamma_{\mathrm{TR}}(\omega, \boldsymbol{k}_{\parallel}) = \frac{1}{\pi\hbar\mu_0\omega^2} \gamma_b (|t_p^+|^2 + |t_s^+|^2 + |t_p^-|^2 + |t_s^-|^2). \qquad (54)$$

Here, we assume that the Cherenkov radiation does not take place outside the slab.

If the slab is dissipation-less, the determinant of the coefficient matrix Eqs. (47) and (48) can have a real zero at a certain $k_{\parallel}$, giving rise to a pole in $c_p^{\pm}, c_s^{\pm}$ as a function of $k_{\parallel}$. This pole corresponds to a guided mode in a dielectric slab and a Ritchie plasmon polariton mode in a metallic slab. In the latter case, only the p-polarization is relevant. The pole gives a delta function in $\Gamma_{\mathrm{EL}}(\omega, \boldsymbol{k}_{\parallel})$ outside the light cone. Thus, by evaluating the pole residue, we can obtain an analytic expression of the excitation efficiency and the angular distribution of the confined mode concerned.

One may wonder whether there is a possibility of the pole due to the Cherenkov radiation being inside the slab. However, this pole is completely canceled in the energy-loss spectrum as well as in the transmission and reflection coefficients.

4. Numerical Results and Discussion

In what follows, we consider doped graphene with the local optical conductivity[25]

$$\sigma(\omega) = \frac{e^2 E_f}{\pi\hbar^2} \frac{i}{\omega + i\tau^{-1}} + \frac{ie^2}{2h} \log_e \left(\frac{2E_f - \hbar(\omega + i\tau^{-1})}{2E_f + \hbar(\omega + i\tau^{-1})} \right), \qquad (55)$$

where E_f is the Fermi energy measured from the Dirac point of graphene and τ is the relaxation time.

The first term in Eq. (55) is the intraband contribution, while the second term is the interband one. At high frequencies, the conductivity saturates as $\sigma(\omega) \simeq e^2/(4\hbar)$, which explains the small optical absorption of 2.3% of graphene. In the plasmon pole approximation, we assume $\tau \to \infty$ and $\hbar\omega < 2E_f$, so that the conductivity is pure imaginary. The deviation in the conductivity from an infinite τ appears strongly at low frequencies $\omega < 1/\tau$. There, the real part of the conductivity becomes dominating, while in the infinite τ limit the real part is zero. Therefore, the pole approximation in this region

is not justified. We should point out here that the conductivity at $\tau \to \infty$ scales with the threshold frequency $\omega_c \equiv 2E_f/\hbar$ of the interband transition. Therefore, from now on, we normalize frequency ω by ω_c.

For comparison, we also consider a thin metallic slab of the Drude permittivity

$$\epsilon_a(\omega) = 1 - \frac{\omega_p^2}{\omega(\omega + i\tau^{-1})}, \qquad (56)$$

free-standing in vacuum. The slab thickness d is taken to be $0.25\lambda_p$, where $\lambda_p (= 2\pi c/\omega_p)$ is the plasma wavelength. The relaxation time τ is assumed to be infinity for the pole approximation, otherwise it is finite. Again, at $\tau \to \infty$, the permittivity scales with ω_p, and thus we normalize frequency ω by ω_p.

In the graphene case, the graphene plasmon polariton plays crucial roles in various optical phenomena. In the metallic slab case, the Ritchie plasmon polariton has profound importance. Their dispersion relations at $\tau \to \infty$ are given in Fig. 2.

In doped graphene, the plasmon-polariton dispersion behaves like $\omega \sim \sqrt{\alpha_e \omega_c c k_{\parallel}}$, with α_e being the fine structure constant, so that it has a broad range of the spectrum controllable by electron doping. In actual systems, however, the interband transition and the nonlocality in the optical conductivity at a large $k_{\parallel}$ strongly affect the plasmon-polariton dispersion. Therefore, when we discuss the plasmon polariton in this paper, we concentrate on the limited frequency range shown in Fig. 2 (a).

In the metallic slab, two plasmon-polariton branches emerge with opposite parities in the z-direction. The lower polariton is, to some extent, similar to the graphene plasmon polariton, while the upper polariton tends to stay at $\omega = \omega_p$ in the infinitely thin slab limit. The eigenfrequencies of the plasmon polaritons approach $\omega = \omega_p/\sqrt{2}$ with increasing $k_{\parallel}$. However, at a large $k_{\parallel}$ the nonlocality in the permittivity becomes important, showing a limitation of the local-response approximation employed in this paper. We thus restrict ourselves in the frequency region below $0.706\omega_p$ when we discuss the Ritchie plasmon polariton.

4.1 Momentum-resolved spectra

First, we consider the map of the momentum-resolved energy-loss and transition-radiation spectra in doped graphene. The map visualizes various features of doped graphene intuitively. Such spectral maps of the energy loss for silicon slabs are found, for instance, in Refs. 26 and 27.

Figure 3 shows the spectral maps for the oblique incidence of the electron beam with different electron velocities. The spectra exhibit two marked domains, namely, above and below the interband transition threshold ($\omega = \omega_c$). The spectra are rather plain above the threshold, whereas they are rich below the threshold. It is remarkable that the plasmon loss indicated by the bright curve below the threshold dominates the energy-loss spectrum especially at lower electron velocities. We also point out that the transition radiation, which can be
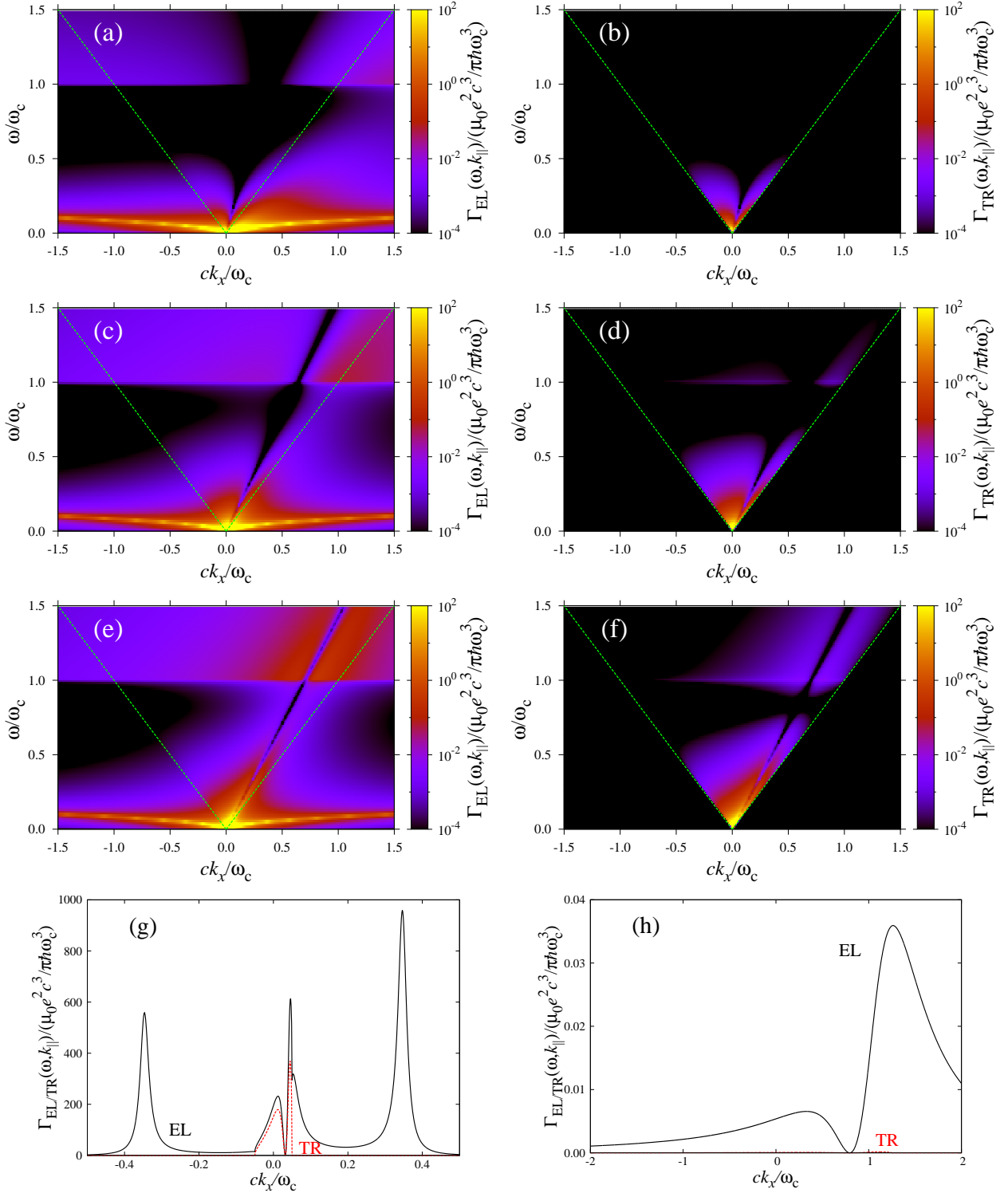
Fig. 3. (Color online) Momentum-resolved energy-loss spectrum $\Gamma_{EL}(\omega, \boldsymbol{k}_\parallel)$ and transition-radiation spectrum $\Gamma_{TR}(\omega, \boldsymbol{k}_\parallel)$ at $k_y = 0$ of doped graphene. The local-response approximation of the optical conductivity is employed. The Fermi energy E_f is assumed to be 0.4 [eV] measured from the Dirac point of graphene. The relaxation time τ is taken to be 4×10^{-13} [s]. An oblique incidence of $\theta_{inc} = \pi/4$ is assumed. The electron velocity is taken to be $v = 0.5c$ (a,b), $0.9c$ (c,d), and $0.99c$ (e,f). Cross-sectional views of these spectra for $v = 0.9c$ at $\omega/\omega_c = 0.05$ and 1.25 are also plotted in (g) and (h), respectively.
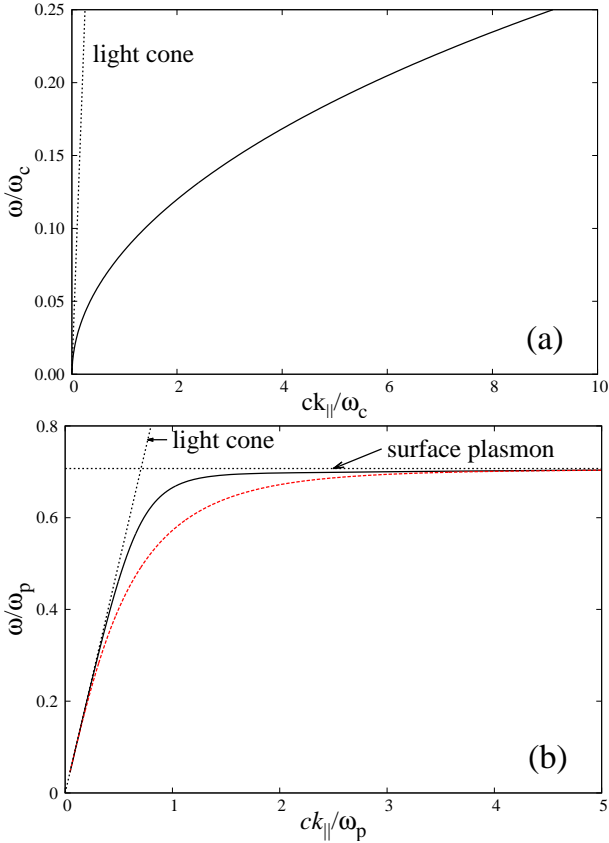
Fig. 2. (Color online) (a) Dispersion relation of the graphene plasmon polariton. The optical conductivity is given by $\sigma(\omega) = ie^2 E_f/(\pi\hbar^2\omega) + ie^2/2\hbar \log_e((2E_f - \hbar\omega)/(2E_f + \hbar\omega))$ with $2E_f = \hbar\omega_c$, where ω_c is the threshold frequency of the interband transition. (b) Dispersion relation of Ritchie plasmon polaritons in a thin metallic film with a thickness $d = \lambda_p/4$ and a Drude permittivity $\epsilon_a(\omega) = 1 - (\omega_p/\omega)^2$, where $\omega_p(= 2\pi c/\lambda_p)$ is the plasma frequency. The background medium is air ($\epsilon_b = 1$) in both cases. The light cone is given by $\omega = ck_\|$. The horizontal dashed line in (b) represents the surface plasmon frequency $\omega = \omega_p/\sqrt{2}$.

Fig. 4. (Color online) (a) Excitation efficiencies of the graphene plasmon polariton at various velocities of the electron beam. The incident angle is fixed to $45°$. (b) Excitation efficiencies at $v = 0.1c$ for various incident angles. The plasmon-pole approximation is employed.

found inside the light cone ($\omega > c|\boldsymbol{k}_\||$), increases in its percentage of the energy loss, and becomes spectrally wide and forward (and backward) oriented with increasing electron velocity. The latter property is common in ordinary transition radiation at the interface between two media with different refractive indices. However, it is not so trivial because we have only one atomic monolayer.

A spectral dip is found along a straight line in the (k_x, ω) plane. The dip is purely kinetic and is given by $\omega = c^2 k_x/v_x$. In this dip, the factor $\boldsymbol{P}_v^t \overleftrightarrow{\alpha}{}^0$ appearing in Eq. (28) vanishes, provided $v_y = k_y = 0$.

Let us have a close look at the spectra relevant to the plasmon-polariton excitation. Figures 3(g) and 3(h) show cross-sectional plots of the spectra at $\omega/\omega_c = 0.05$ and 1.25, respectively, for $v = 0.9c$. At $\omega/\omega_c = 0.05$, several peaks are found in the energy-loss spectrum. Among them, the two peaks found at $ck_x/\omega_c \sim \pm 0.35$ are due to the plasmon-polariton excitation. The others are due to the transition radiation. Figure 3(g) indicates that, if the plasmon polariton is relevant in the frequency range concerned, most of the energy loss is taken away by the plasmon polariton. The transition radiation gives a rather small contribution to the energy loss. However, there is a certain region at approximately $k_x = 0$ in which the momentum-resolved energy loss is domi-
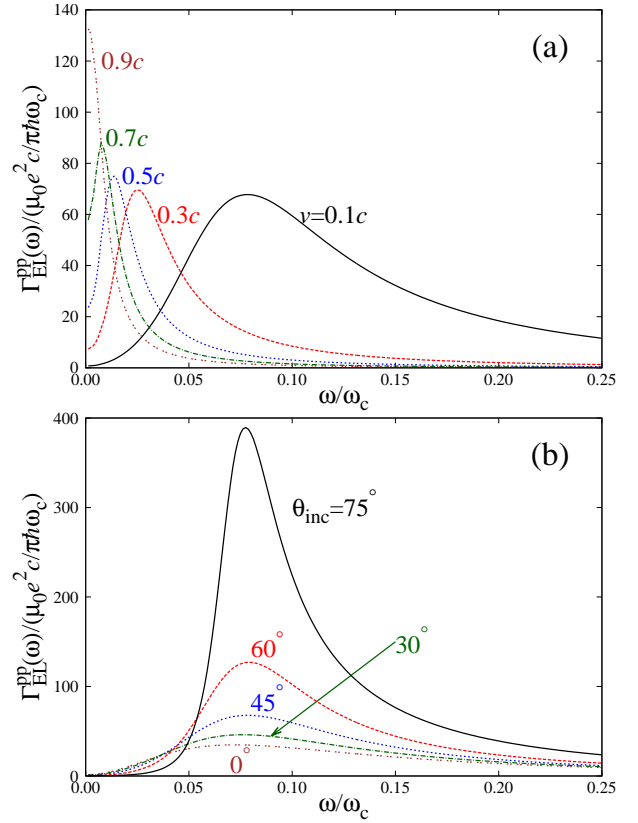
nated by the transition radiation. We also find, as in Fig. 3(h), that, above the interband threshold, most of the energy loss is caused by the dissipation due to the real part of the conductivity tensor $\Re[\sigma] \simeq e^2/4\hbar$.

We should note, however, that, if the dissipation is completely absent, the momentum-resolved energy-loss spectrum coincides with that of the transition-radiation spectrum inside the light cone. Outside the light cone, the former exhibits the delta-function singularity at the plasmon-polariton dispersion $k_\| = k_\|^{\mathrm{pp}}(\omega)$, otherwise it is zero. The latter vanishes outside the light cone. By numerical calculation, we can see that the transition-radiation spectrum in dissipative systems is not markedly different from that in dissipation-less systems.

4.2 Plasmon excitation efficiency

Next, we consider the excitation efficiency of the plasmon polariton. We employ the plasmon-pole approximation, in which the dissipation (that is, the real part of the conductivity) is neglected ($\tau \to \infty$ and $\hbar\omega < 2E_f$). Generally, the dissipation makes sharp peaks and dips of the energy-loss spectrum rounder, while their integrals show a small change. The spectrum itself in off-resonance regions shows a small change with the dissipation. Therefore, we should note that the plasmon-pole approximation tends to overestimate possible spectral peaks.

Figure 4 shows the excitation efficiency of the plasmon polariton by the electron beam of the oblique incidence. Note that the peak of the excitation efficiency exhibits a red shift and becomes narrow with increasing velocity of the elec-
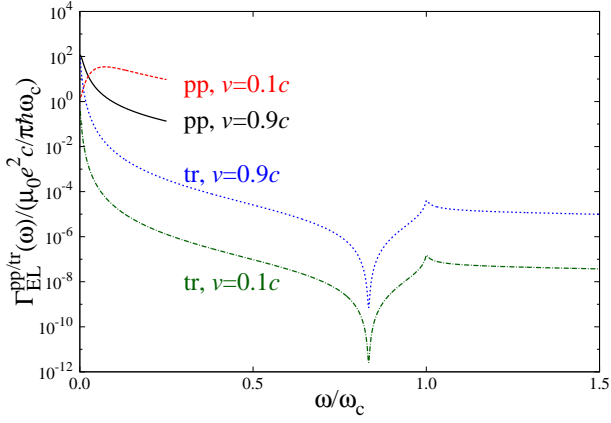
Fig. 5. (Color online) Comparison between the plasmon-polariton excitation rate $\Gamma_{EL}^{pp}(\omega)$ and the transition-radiation rate $\Gamma_{EL}^{tr}(\omega)$ in doped graphene. The normal incidence of the electron beam is assumed.
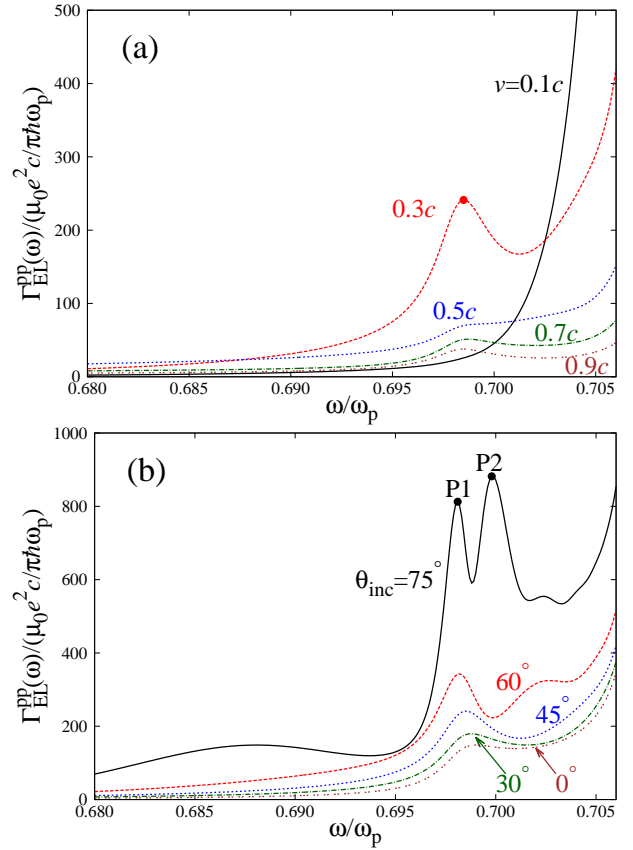

Fig. 6. (Color online) Excitation rate of the Ritchie plasmon polaritons in a thin metallic film of thickness $d = \lambda_p/4$. The frequency range close to the surface plasmon frequency $\omega_p/\sqrt{2}$ is considered. (a) Velocity dependence of the excitation rate. The incident angle is fixed to $45°$. (b) Incident angle dependence. The electron velocity is fixed to $v = 0.3c$.

tron beam. Conversely, a slower electron excites the graphene plasmon polariton in a higher and wider frequency range. These properties are reasonable because, at high frequencies, the plasmon-polariton dispersion is far from the light cone, so that the polariton can be dealt well with the nonretardation (quasi-static) approximation in which the light velocity c is taken to be infinity. The electron velocity is then negligible compared with the light velocity.

As for the incident angle dependence, a highly efficient excitation is achieved at the oblique incidence with a large incident angle. This property is reminiscent of the excitation of the surface plasmon polariton in the attenuated total-reflection setup.[28] In the setup, an evanescent light is incident through prism coupling. The electric field accompanied by the electron beam is also evanescent away from the electron trajectory. As an extreme oblique incidence, properties of the plasmon excitation are summarized in Appendix, for the electron traveling parallel to graphene.

As shown in the previous subsection, the energy loss of the electron transmitted through graphene is mainly caused by the excitation of the graphene plasmon polariton. However, at low frequencies, the plasmon-polariton dispersion curve remains near the light cone, as shown in Fig. 2(a), so that the resulting wave is lightlike. As a consequence, the transition radiation becomes non-negligible there. Figure 5 shows the comparison between the plasmon-polariton excitation rate and the transition-radiation rate for the normal incidence. Note that the vertical axis is given on the logarithmic scale. Therefore, for $v = 0.1c$, the transition-radiation rate is much lower, of order 10^{-7}, than the plasmon-polariton excitation rate at $\omega/\omega_c = 0.25$. Even for $v = 0.9c$, the transition-radiation rate is two orders of magnitude lower than the plasmon-polariton excitation rate at the same frequency. Generally, the transition-radiation rate becomes larger for a faster electron, a smaller incident angle, and a lower frequency. Therefore, we can see that the transition-radiation rate of the normally incident electron beam with $v = 0.9c$ becomes on the same order as the plasmon-polariton excitation rate at very low frequencies.

Above the frequency $\omega/\omega_c = 0.25$, the momentum of the plasmon polariton exceeds $\hbar c k_\parallel/\omega_c \sim 10$, as shown in Fig. 2(a). If the Fermi energy E_f is set at 0.4 [eV], $\hbar c k_x$ reaches 8 [eV], which is in the far-ultraviolet region, so that the local-

response approximation for the conductivity becomes worse. On the other hand, we can reasonably evaluate the transition-radiation rate $\Gamma_{TR}(\omega)$ there, because relevant momenta are inside the light cone, bounded as $k_\parallel < \omega/c$.

Figure 5 also shows the transition-radiation rate up to $\omega/\omega_c = 1.5$. The sharp dip at $\omega/\omega_c \sim 0.84$ in Fig. 5 is due to the zero of the conductivity in Eq. (55). Therefore, the transition radiation through doped graphene vanishes. We can also find a small peak of the transition-radiation rate at the threshold of the interband transition, $\omega = \omega_c$. This peak grows with increasing velocity. We will discuss the transition radiation there in the next subsection.

For comparison, we consider the excitation rate of plasmon polaritons in a thin metallic film. Figure 6 shows the spectrum of the excitation rate for various velocities and incident angles. Here, we restrict ourselves in the frequency range up to $0.706\omega_p$, which is close to the surface plasmon frequency $\omega_p/\sqrt{2}$. Above the frequency bound, the momentum $k_\parallel$ of the plasmon polariton exceeds $10\omega_p/c$. Since the plasma frequency is on the order of several electron volts, the local-response approximation employed in this study becomes worse in such a range.

In a metallic slab, the excitation rate of plasmon polaritons generally increases with increasing frequency toward $\omega_p/\sqrt{2}$. We also find spectral fringes due to the interference between two plasmon polaritons with different parities. The spectral intensity and fringe become remarkable for a large incident
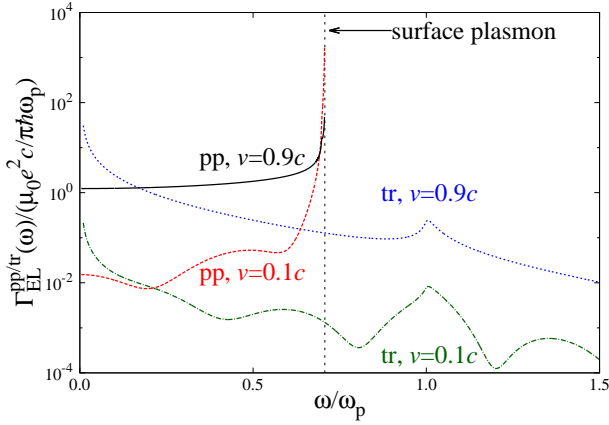
Fig. 7. (Color online) Excitation rate of the Ritchie plasmon polaritons and the transition-radiation rate in a thin metallic film of $d = \lambda_p/4$. A normal incidence of the electron beam is assumed. The dashed line indicates the surface plasmon frequency $\omega = \omega_p/\sqrt{2}$.

angle, particularly at $v = 0.3c$. Above $\omega_p/\sqrt{2}$, the excitation rate vanishes, because there is no plasmon-polariton dispersion.

A remarkable contrast to doped graphene is afforded for the limited tunability of the plasmon-polariton excitation. That is, no marked peak in the excitation rate is found below $\omega = 0.68\omega_p$ even if the velocity and incident angle are varied. This property implies that, in the thin metallic slab, plasmon polaritons at low frequencies are not efficiently excited by the electron beam. An efficient excitation is limited only near the surface plasmon frequencies.

As for the transition radiation of the metallic slab, a significant portion of the electron energy loss is taken away by the transition radiation, particularly at low frequencies. Figure 7 shows a comparison between the excitation rate of the plasmon polaritons and the transition-radiation rate. We can find a crossover between the plasmon-polariton excitation rate and the transition-radiation rate at $\omega/\omega_p \sim 0.2$. Below this frequency, the transition radiation dominates in the energy loss. The transition-radiation rate exhibits a small peak at the bulk plasmon frequency $\omega = \omega_p$. These features are independent of the incident angle and electron velocity.

4.3 Angular distribution of plasmon polariton and transition radiation

Finally, we consider the angular distribution of the plasmon polariton and the transition radiation. Again, the plasmon-pole approximation is employed.

In the normal-incidence case the angular distribution of the plasmon polariton is isotropic by the rotational symmetry with respect to the electron trajectory. Therefore, a selective excitation of the graphene plasmon polariton at a particular momentum $\boldsymbol{k}_{\parallel}$ is not available. However, if the incident angle is tilted, the angular distribution is deformed from a circular-symmetric shape, giving rise to the possible control of the plasmon-polariton excitation.

Figure 8 shows the angular distribution of the graphene plasmon polariton excited by electron beams at the peak frequencies in Fig. 4. We can see that, when the incident angle is fixed to 45°, the angular distribution does not change markedly with varying velocity. We also find that for a larger
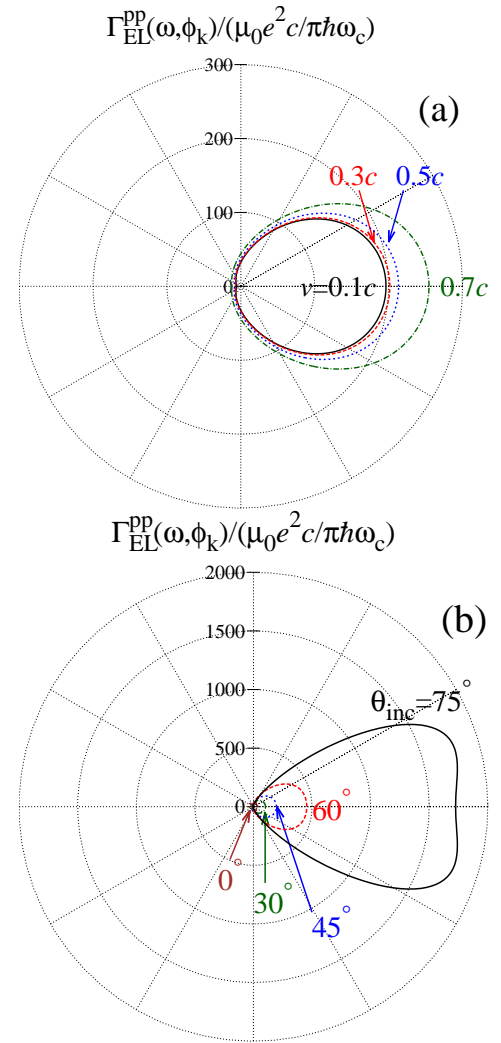

Fig. 8. (Color online) Angular distribution of the graphene plasmon polariton at the peak frequencies of the plasmon-polariton excitation rate in Fig. 4. The incident azimuthal angle ϕ_{inc} is fixed to 0° (tilted in the x-direction). (a) At the peak frequencies in Fig. 4(a). The incident (polar) angle is fixed to 45°. (b) At the peak frequencies in Fig. 4(b). The velocity is fixed to $v = 0.1c$.

incident angle, the directivity and excitation efficiency of the plasmon polariton increase. However, even at $\theta_{\mathrm{inc}} = 75°$, the angular distribution still has a rather large deviation of $\Delta\phi_k \sim \pm30°$. A similar property is obtained at the peak frequency of the excitation efficiency for other velocities. Therefore, the controllability of the momentum of the plasmon polariton is limited.

As for the transition radiation, the spectral peak is found at the threshold of the interband transition, as shown in Fig. 5. For a normally incident electron beam of $v = 0.9c$ and $0.99c$, the angular distribution of the transition radiation at the threshold is shown in Fig. 9. Here, we plotted the polar-angle distribution. By the rotational symmetry there is no azimuthal angle dependence. The angular distribution exhibits strong forward- and backward-oriented profiles at ultrarelativistic velocities, which is typical of the transition radiation for relativistic electron beams. The directivity and intensity in the forward and backward orientations increase with increasing velocity of the electron beam.

For comparison, we consider the angular distribution of plasmon polaritons in a thin metallic slab. Figure 10 shows
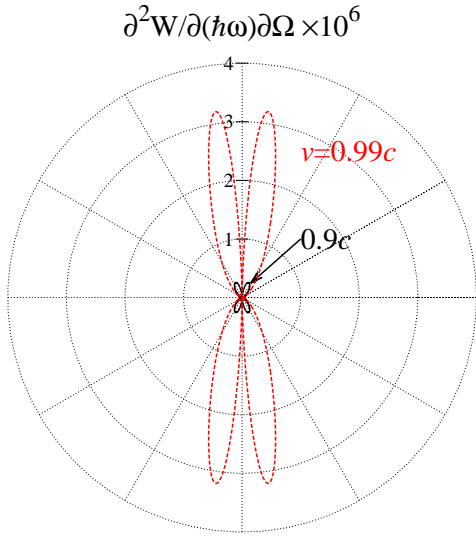
$$\partial^2 W/\partial(\hbar\omega)\partial\Omega \times 10^6$$

Fig. 9. (Color online) Angular distribution of the transition radiation at the interband transition threshold. A normal incidence is assumed.

the angular distribution of two plasmon polaritons at the peak frequencies in Fig. 6. Since the two plasmon polaritons are excited, we can consider the angular distribution of each polariton. The angular distributions exhibit nodal structures, in which there are several $k_{\parallel}$ points at given frequencies such that the plasmon polaritons are not excited. By numerical calculation, we can show that the number of nodes increases with increasing frequency toward $\omega_p/\sqrt{2}$. In addition, we also find that, for a larger incident angle, the directivity and intensity of the plasmon-polariton excitation increase. For instance, at $\theta_{\text{inc}} = 75°$, the upper polariton mode is dominantly excited by the electron beam of $v = 0.3c$. It has broad peaks in the angular distribution at $\phi_k \sim \pm 22°$. The lower polariton mode exhibits sharp peaks in the angular distribution at $\phi_k \simeq 45°$, although its intensity is lower than that of the upper polariton mode. In this way, the excitation of the Ritchie plasmon polaritons near the surface-plasmon frequency can be controlled by the electron beam fairly well.

5. Conclusions

We have presented a detailed theoretical analysis of the interaction between an electron beam and doped graphene under the local-response approximation. An electron incident on doped graphene induces the out-of-plane transition radiation and in-plane plasmon-polariton waves. The rates of the plasmon-polariton excitation and transition radiation are quantitatively evaluated and compared with those of a thin metallic slab. The plasmon polariton in doped graphene has a controllable spectrum of the $\sqrt{k_{\parallel}}$-type dispersion relation. We have observed that there is an appropriate velocity of the electron beam that very efficiently excites the plasmon polariton of particular frequency in the broad frequency range. In contrast, for the metallic slab, the efficient excitation of the plasmon polariton is limited near the surface plasmon frequency $\omega_p/\sqrt{2}$. A deeply tilted incidence is better for the excitation of the graphene plasmon polariton. The resulting angular distribution of the graphene plasmon polariton has a rather large deviation of $\pm 30°$. We have also observed that the transition radiation in doped graphene exhibits a small peak at the interband-transition threshold.
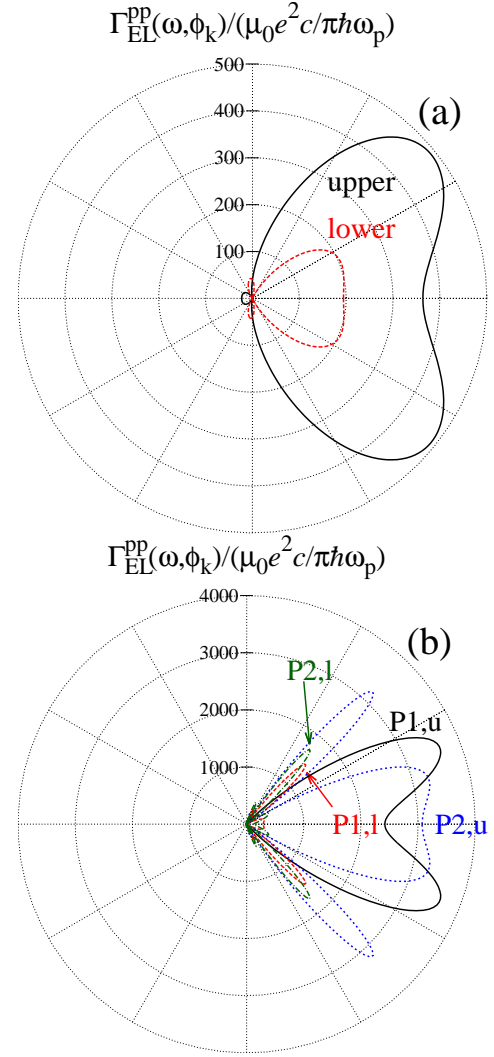
$$\Gamma_{\text{EL}}^{\text{pp}}(\omega,\phi_k)/(\mu_0 e^2 c/\pi\hbar\omega_p)$$

$$\Gamma_{\text{EL}}^{\text{pp}}(\omega,\phi_k)/(\mu_0 e^2 c/\pi\hbar\omega_p)$$

Fig. 10. (Color online) Angular distribution of the Ritchie plasmon polaritons at the peak frequencies in Fig. 6. The incident azimuthal angle ϕ_{inc} is fixed to $0°$. (a) At the peak frequency marked in Fig. 6(a) ($v = 0.3c$ and $\theta_{\text{inc}} = 45°$). The term "upper (lower)" indicates the contribution of the upper (lower) polariton given in Fig. 2(b). (b) At the peak frequencies(P1 and P2) marked in Fig. 6 b ($v = 0.3c$ and $\theta_{\text{inc}} = 75°$). The term "P1,u(l)" stands for the contribution of the upper (lower) polariton at P1, for instance.

Appendix

Here, we present an extreme case of an oblique-incident electron beam, namely, an electron traveling parallel to graphene. In this case, no transition radiation emerges, and the energy loss of the traveling electron is caused only by the plasmon-polariton excitation and absorption. The energy-loss rate is proportional to the length of the electron trajectory. Therefore, it can be arbitrarily large by assuming an appropriately long trajectory. Thus, direct comparison to the transmitted setup of the electron beam through graphene is not available.

Suppose that an electron is traveling in the x-direction above a graphene sheet with a distance d. The evanescent
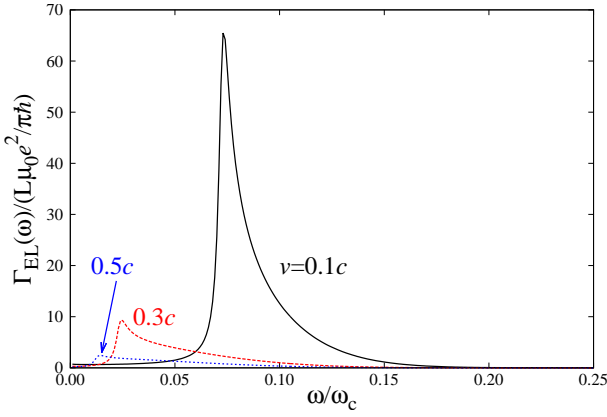
Fig. A·1. (Color online) Electron energy-loss spectrum for an electron traveling parallel to doped graphene with dissipation ($E_f = 0.4$ [eV] and $\tau = 4 \times 10^{-13}$ [s]). The distance between the electron trajectory and graphene is taken to be $d = 0.1 \times 2\pi c/\omega_c \sim 155$ [nm], and L is the length of the electron trajectory.

wave accompanied by the traveling electron is written as

$$\boldsymbol{E}^0(\boldsymbol{x}; \omega) = \int \frac{dk_y}{2\pi} \boldsymbol{E}_k^{0\pm}(\omega) e^{i\boldsymbol{K}_b^{\pm} \cdot \boldsymbol{x}}, \tag{A·1}$$

$$\boldsymbol{E}_k^{0\pm}(\omega) = -\frac{\mu_0 e \omega}{2\gamma_b} \boldsymbol{P}_x^{\pm} e^{\mp i \gamma_b d}, \tag{A·2}$$

$$\boldsymbol{P}_x^{\pm} = \left(\overleftrightarrow{1} - \frac{1}{q_b^2} \boldsymbol{K}_b^{\pm} \otimes \boldsymbol{K}_b^{\pm} \right) \hat{x}. \tag{A·3}$$

Here, in the definition of $\boldsymbol{K}_b^{\pm}$ given in Eq. (13), k_x is replaced with ω/v, with v as the electron velocity. Using the Rayleigh-scattering formula found in Sect. 2.1, the electron energy-loss spectrum is given by

$$\Gamma_{\text{EL}}(\omega) = \int \frac{dk_y}{2\pi} \Gamma_{\text{EL}}(\omega, k_y), \tag{A·4}$$

$$\Gamma_{\text{EL}}(\omega, k_y) = -\frac{\mu_0 e^2 L}{2\pi\hbar} \Re \left[(\boldsymbol{P}_x^+)^t \overleftrightarrow{\tilde{\alpha}}_k \boldsymbol{P}_x^- \frac{1}{\gamma_b} e^{2i\gamma_b d} \right], \tag{A·5}$$

where $\Gamma_{\text{EL}}(\omega, k_y)$ is the differential probability of energy loss $\hbar\omega$ and momentum transfer $\hbar k_y$ in the y-direction, and L is the length of the electron trajectory.

In the dissipation-less limit, $\Gamma_{\text{EL}}(\omega, k_y)$ becomes the delta function on the plasmon polariton dispersion $\sqrt{(\omega/v)^2 + k_y^2} = k_{\parallel}^{\text{pp}}(\omega)$. By solving this equation with respect to ω, we obtain the modified band structure $\omega = \omega_{\text{pp};v}(k_y)$ as a function of k_y. Thus, we analytically calculate the excitation rate of the graphene plasmon polariton. Even if the dissipation is taken into account, the excitation rate can be evaluated easily by the Sommerfeld integral[22] over k_y. The result for dissipative

graphene is shown in Fig. A·1. The energy-loss spectrum exhibits a peak at the frequency bottom of the modified band structure of the plasmon polariton. The bottom is found at $k_y = 0$, so that its frequency is obtained as a cross point between the dispersion curve $|k_x| = k_{\parallel}^{\text{pp}}(\omega)$ and $k_x = \omega/v$. As we can see, a slower electron more efficiently excites the plasmon polariton at higher frequencies. The resulting plasmon polariton at the peak frequency has $k_y = 0$ and thus propagates in the direction parallel to the traveling electron.

1) E. Ozbay, Science **311**, 189 (2006).
2) D. K. Gramotnev and S. I. Bozhevolnyi, Nature Photon. **4**, 83 (2010).
3) D. Bohm and D. Pines, Phys. Rev. **92**, 609 (1953).
4) H. Raether, *Surface Plasmons on Smooth and Rough Surfaces and on Gratings* (Springer-Verlag, Berlin, 1988), Chap. 2.
5) L. Ju, B. Geng, J. Horng, C. Girit, M. Martin, Z. Hao, H. A. Bechtel, X. Liang, A. Zettl, Y. R. Shen, and F. Wang, Nat. Nanotechnol. **6** 630 (2011).
6) S. Thongrattanasiri, F. H. L. Koppens, and F. J. García de Abajo, Phys. Rev. Lett. **108**, 047401 (2012).
7) F. H. L. Koppens, D. E. Chang, and F. J. García de Abajo, Nano Lett. **11**, 3370 (2011).
8) R. F. Egerton: *Electron energy-loss spectroscopy in the electron microscope* (Springer, New York, 2011) 3rd ed., Chap. 1.
9) F. J. García de Abajo, Rev. Mod. Phys. **82**, 209 (2010).
10) M. Kuttge, E. J. R. Vesseur, A. F. Koenderink, H. J. Lezec, H. A. Atwater, F. J. García de Abajo, and A. Polman, Phys. Rev. B **79**, 113405 (2009).
11) M. Honda and N. Yamamoto, Opt. Express **21**, 11973 (2013).
12) A. L. Koh, A. I. Fernandez-Dominguez, D. W. McComb, S. A. Maier, and J. K. W. Yang, Nano Lett. **11**, 1323 (2011).
13) D. Rossouw, M. Couillard, J. Vickery, E. Kumacheva, and G. A. Botton, Nano Lett. **11**, 1499 (2011).
14) O. Nicoletti, M. Wubs, N. A. Mortensen, W. Sigle, P. A. van Aken, and P. A. Midgley, Opt. Express **19**, 15371 (2011).
15) V. Ginzburg and I. M. Frank, Sov. Phys. JETP **16**, 15 (1946).
16) P. A. Cherenkov, Dokl. Akad. Nauk SSSR **2**, 451 (1934).
17) S. J. Smith and E. M. Purcell, Phys. Rev. **92**, 1069 (1953).
18) G. W. Ford and W. H. Weber, Phys. Rep. **113**, 195 (1984).
19) A. Wokaun, J. P. Gordon, and P. F. Liao, Phys. Rev. Lett. **48**, 957 (1982).
20) J. D. Jackson, *Classical Electrodynamics* (Wiley, New York, 1998) 3rd ed., p. 633.
21) We should note that, in Eq. (26), the electric field $\boldsymbol{E}$ must include the direct term $\boldsymbol{E}^0$ produced by the electron itself. Otherwise, the Cherenkov loss in the background medium, which is nonzero if $|v| > c/\sqrt{\epsilon_b}$, cannot be derived.
22) W. C. Chew, *Waves and Fields in Inhomogeneous Media* (IEEE Press, New York, 1995), Chap. 2.
23) R. H. Ritchie, Phys. Rev. **106**, 874 (1957).
24) J. E. Sipe, J. Opt. Soc. Am. B **4**, 481 (1987).
25) V. P. Gusynin, S. G. Sharapov, and J. P. Carbotte, Phys. Rev. B **75**, 165407 (2007).
26) C. H. Chen, J. Silcox, and R. Vincent, Phys. Rev. B **12**, 64 (1975).
27) A. Yurtsever, M. Couillard, and D. A. Muller, Phys. Rev. Lett. **100**, 217402 (2008).
28) E. Kretschmann and H. Raether, Z. Naturforsch. A **23**, 2135 (1968).